# Large tunability of lattice thermal conductivity of monolayer silicene via mechanical strain

Han Xie,[1] Tao Ouyang,[2] Éric Germaneau,[3] Guangzhao Qin,[2] Ming Hu,[2,4,*] and Hua Bao[1,†]
[1]*University of Michigan–Shanghai Jiao Tong University Joint Institute, Shanghai Jiao Tong University, Shanghai 200240, China*
[2]*Institute of Mineral Engineering, Division of Materials Science and Engineering, Faculty of Georesources and Materials Engineering, RWTH Aachen University, Aachen 52064, Germany*
[3]*Center for High Performance Computing, Shanghai Jiao Tong University, Shanghai 200240, China*
[4]*Aachen Institute for Advanced Study in Computational Engineering Science (AICES), RWTH Aachen University, Aachen 52062, Germany*
(Received 2 September 2015; revised manuscript received 2 January 2016; published 2 February 2016)

Strain engineering is one of the most promising and effective routes toward continuously tuning the electronic and optic properties of materials, while thermal properties are generally believed to be insensitive to mechanical strain. In this paper, the strain-dependent thermal conductivity of monolayer silicene under uniform biaxial tension is computed by solving the phonon Boltzmann transport equation with interatomic force constants extracted from first-principles calculations. Unlike the commonly believed understanding that thermal conductivity only slightly decreases with increased tensile strain for bulk materials, it is found that the thermal conductivity of silicene can increase dramatically with strain. Depending on the size, the maximum thermal conductivity of strained silicene can be a few times higher than that of the unstrained case. Such an unusual strain dependence is mainly attributed to the dramatic enhancement in the acoustic phonon lifetime. Such enhancement plausibly originates from the flattening of the buckling of the silicene structure upon stretching, which is unique for silicene as compared with other common two-dimensional materials. Our findings offer perspectives on modulating the thermal properties of low-dimensional structures for applications such as thermoelectrics, thermal circuits, and nanoelectronics.

DOI: 10.1103/PhysRevB.93.075404

## I. INTRODUCTION

Two-dimensional (2D) materials have been extensively studied in the past decade because of their novel physical and chemical properties [1–3] and potential applications [4,5]. For example, it has been found that graphene has extremely high thermal conductivity [6], which has great potential in applications including electronic cooling and composite materials. Silicene is the silicon counterpart of graphene and another typical 2D material with a honeycomb lattice structure. Compared to graphene, silicene is more compatible with silicon-based semiconductor technology and therefore has greater potential in nanoelectronic applications. Silicene has also been found to have opened a tunable band gap when a transverse electric field is applied [7–9]. Monolayer silicene has been successfully fabricated on substrates such as Ag(110) [10], Ir(111) [11], and Ag(111) [12] surfaces. Recently, Tao *et al.* have demonstrated silicene transistors operating at room temperature [5]. Although the performance is still moderate and the lifetime of this transistor is only a few minutes, it has attracted significant research interest in silicene-based devices [13–15].

On the other hand, the intrinsic physical properties of silicene, such as lattice thermal conductivity, have been an active area of research. Although the thermal conductivity of silicene has not been measured in experiments due to the difficulty of synthesizing freestanding silicene, several numerical simulations have predicted the thermal conductivity of silicene and the results at 300 K range from 5 to 69 W/mK [16–21]. Most of the numerical simulations are based on classical molecular dynamics and the discrepancy of results mainly arises from the different interatomic interaction potentials used. Notably, first-principles-based lattice dynamics predicted that the thermal conductivity of silicene is in the range of 20–30 W/mK [21], which should be more reliable. In our previous first-principles calculations [20], the thermal conductivity of 9.4 W/mK at 300 K was not refined due to the small cutoff used for the anharmonic force constant calculation and not imposing the sum rule [22]. Our new calculation results are consistent with the one by Gu and Yang [21]. Despite recent efforts to describe the properties of unstrained silicene, in real applications, nanoscale devices usually contain residual strain after fabrication [23]. It is thus important to investigate possible strain effects on the properties of silicene. It was found that a mechanical tensile strain less than 5% could tune the electronic structure of silicene [24] and larger tensile strain (7.5%) could induce a semimetal-metal transition [25]. On the other hand, using first-principles it has been demonstrated that the silicene structure remains buckled even when 12.5% tensile strain is applied [25,26].

In comparison to the structural and electronic properties, the strain effect on the lattice thermal conductivity of silicene is less investigated. Pei *et al.* [18] and Hu *et al.* [19] investigated the effect of uniaxial strain on the thermal conductivity based on the classical nonequilibrium molecular dynamics method. Pei *et al.* studied tensile strain up to 12% and concluded that the thermal conductivity first increases slightly (around 10% increment) and then decreases with an increased amount of tensile strain. Hu *et al.* found that the thermal conductivity of silicene sheet and silicene nanoribbon experiences monotonic increase by a factor of 2 with tensile strain up to 18%. The modified embedded-atom method (MEAM) [27] and original Tersoff potential [28] were used in their simulations, respectively. However, both potentials are developed for bulk

---

[*] Author to whom correspondence should be addressed: hum@ghi.rwth-aachen.de

[†] Author to whom correspondence should be addressed: hua.bao@sjtu.edu.cn

silicon, so directly applying those potentials to the new 2D silicene structure is questionable. For example, the Tersoff potential cannot even reproduce the buckled structure of silicene and the MEAM potential seems to overestimate the buckling distance. It is well known that the interatomic potential directly determines the quality of classical molecular dynamics simulation. Therefore, in order to precisely predict the strain effect on the lattice thermal conductivity of silicene and identify the underlying mechanism, it is necessary to calculate the lattice thermal conductivity of silicene under different strains using a more accurate method.

In this paper, the strain-dependent thermal conductivity of monolayer silicene is calculated based on the single-mode relaxation time approximation (RTA) and iterative solution of the Boltzmann transport equation (BTE), where the harmonic and anharmonic interatomic force constants (IFCs) are determined using first-principles calculations. The contributions of different modes under different strains are analyzed. The governing mechanisms are analyzed and compared with other materials.

## II. METHODS AND SIMULATION DETAILS

From the solution of the BTE, the lattice thermal conductivity in the $x$ direction is obtained as [29]

$$k_l^{xx} = \frac{1}{k_B T^2 \Omega N} \sum_\lambda f_0(f_0+1)(\hbar\omega_\lambda)^2 v_{x,\lambda} F_{x,\lambda}, \tag{1}$$

where $k_B$, $T$, $\Omega$, and $N$ are Boltzmann constant, temperature, the volume of the unit cell, and the number of $q$ points in the first Brillouin zone, respectively. The sum goes over phonon mode $\lambda$ that consists of both wave vector $q$ and phonon branch $\nu$. $f_0$ is the equilibrium Bose-Einstein distribution function. $\hbar$ is the reduced Planck constant. $\omega_\lambda$ is the phonon frequency, and $v_{x,\lambda}$ is the phonon group velocity in the $x$ direction. The last term $F_{x,\lambda}$ is expressed in Ref. [29] as

$$F_{x,\lambda} = \tau_\lambda(v_{x,\lambda} + \Delta_\lambda), \tag{2}$$

where $\tau_\lambda$ is the phonon RTA lifetime. $\Delta_\lambda$ is a correction term that eliminates the inaccuracy of RTA by iteratively solving BTE. When $\Delta_\lambda$ is equal to zero, the RTA result for thermal conductivity is obtained. Equation (1) can be rearranged with the expression for volumetric phonon specific heat [30] $c_{ph}$ and the RTA result for thermal conductivity becomes

$$k_l^{xx} = \frac{1}{N} \sum_\lambda c_{ph,\lambda} v_{x,\lambda}^2 \tau_\lambda. \tag{3}$$

The thermal conductivity accumulation function is defined as the contribution to thermal conductivity by phonons with mean free path less than $\Lambda_0$, which is expressed as

$$k_{acc}(\Lambda_0) = \frac{1}{N} \sum_\lambda^{v_{x,\lambda}\tau_\lambda < \Lambda_0} c_{ph,\lambda} v_{x,\lambda}^2 \tau_\lambda. \tag{4}$$

When the phonon-phonon scattering, isotope scattering, and boundary scattering are considered, the RTA lifetime $\tau_\lambda$ can be computed according to the Matthiessen rule [31]:

$$\frac{1}{\tau_\lambda} = \frac{1}{\tau_\lambda^{ph}} + \frac{1}{\tau_\lambda^{\mathrm{iso}}} + \frac{1}{\tau_\lambda^{b}}. \tag{5}$$

The phonon-phonon lifetime for a three-phonon scattering process is computed as the inversion of the intrinsic scattering rate [29]:

$$\tau_\lambda^{ph} = \frac{1}{\Gamma_\lambda} = N\left(\sum_{\lambda'\lambda''} \Gamma^{+}_{\lambda\lambda'\lambda''} + \frac{1}{2}\sum_{\lambda'\lambda''} \Gamma^{-}_{\lambda\lambda'\lambda''}\right)^{-1}, \tag{6}$$

where $\lambda'$ and $\lambda''$ denote the second and third phonon mode that scatter with phonon mode $\lambda$. $\Gamma^{+}_{\lambda\lambda'\lambda''}$ and $\Gamma^{-}_{\lambda\lambda'\lambda''}$ are the intrinsic three-phonon scattering rates for absorption processes $\lambda + \lambda' \rightarrow \lambda''$ and emission processes $\lambda \rightarrow \lambda' + \lambda''$, respectively. The boundary scattering is the only term that depends on the direction of the phonon group velocity explicitly, which can be expressed as [32]

$$\tau_\lambda^{b} = \frac{L_x}{2|v_{x,\lambda}|}, \tag{7}$$

where $L_x$ is the distance between the two boundaries in $x$ direction. For more details about the method we refer the reader to Refs. [29–32]. Both RTA and iterative method are used to predict thermal conductivity in our calculation.

First-principles calculations were carried out using the VASP package [33]. In all our calculations, we used the projector augmented-wave method [34] and the Perdew-Burke-Ernzerhof (PBE) exchange and correlation [35]. A large energy cutoff of 400 eV was chosen. A vacuum spacing of 15 Å was used to prevent interactions between layers. The electronic stopping criterion was $10^{-8}$ eV. The hexagonal symmetry was enforced during the geometry optimization. A hexagonal primitive unit cell was first generated and optimized with a $30 \times 30 \times 1$ $k$ mesh for electronic integration, and then a $5 \times 5 \times 1$ supercell was built and re-optimized with a $6 \times 6 \times 1$ $k$ mesh until the modulus of the force acting on each atom was less than $1.6 \times 10^{-5}$ eV/Å. For unstrained silicene, the external pressure in the $xy$ plane was $-0.02$ kB after supercell optimization. The supercell was then used to compute the harmonic IFCs required for the phonon dispersion calculation. We used the Phonopy package [36] to compute and diagonalize the dynamical matrix and obtain the phonon dispersion curve. The anharmonic IFCs were extracted using the code from ShengBTE package [29] called THIRDORDER.PY. For this calculation, up to the fourth-nearest neighbors were considered. THIRDORDER.PY also applies the sum rules to the anharmonic IFCs. Finally, we use the ShengBTE package to compute the thermal conductivity in the $x$ direction with the harmonic and anharmonic IFCs. Up to a $201 \times 201 \times 1$ $q$ mesh, which samples the first Brillouin zone, was tested for our phonon-scattering calculation. A thickness of 4.2 Å, which is twice the van der Waals radius of the silicon atom, were considered. Isotope scattering with the natural isotopic distribution of silicon was considered when solving the BTE, as implemented in ShengBTE. We also tested all the unstrained and strained cases without isotope scattering and the results were quite similar. Boundary scattering was taken into consideration in the $x$ direction. We added the boundary scattering term by modifying the original ShengBTE code. For the strained structures we proceeded in the same way. They were however optimized with a fixed strained lattice constant. Strained structures were generated by stretching the lattice constant $a$ and the width in the $x$ direction $L_x$ by a

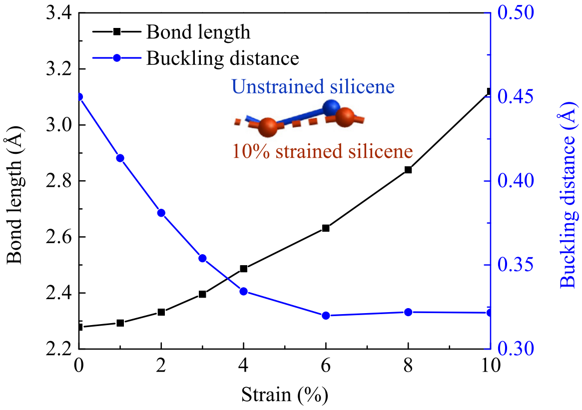

FIG. 1. Bond length and buckling distance as a function of strain. Inset: Primitive unit cell structures for unstrained and 10% strained silicene.

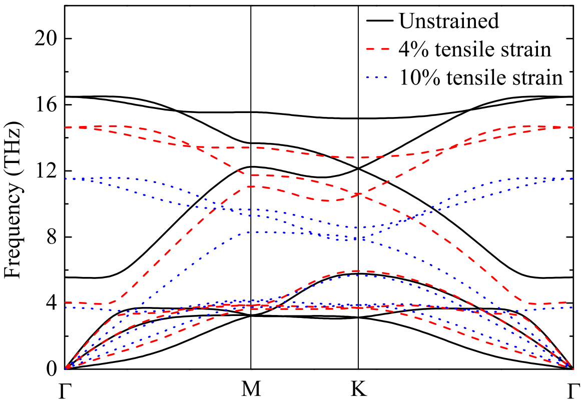

FIG. 2. Phonon dispersion curves of unstrained silicene and strained silicene under 4% and 10% tensile strain.

certain percentage $\epsilon = (a^{\epsilon} - a^0)/a^0 = (L_x^{\epsilon} - L_x^0)/L_x^0$, where the superscript $\epsilon$ denotes the applied strain in strained silicene and 0 denotes unstrained silicene.

## III. RESULTS AND DISCUSSION

### A. Structure

The optimized lattice constant of unstrained silicene is 3.87 Å. Figure 1 shows the Si-Si bond length and buckling distance of silicene as a function of strain. The buckling distance first decreases significantly with increasing strain from 0% to 4%, and then decreases slowly from 4% to 6%, and finally stays almost unchanged from 6% to 10%. The small fluctuation from 6% to 10% strain can be attributed to numerical uncertainty. On the other hand, the Si-Si bond length keeps increasing when strain becomes larger. This result is similar to previous first-principles calculations [25]. It is known that $\pi$ bonding is weaker in silicene than that in graphene because of the longer bond distance. The $sp^2$ bonding will be dehybridized into $sp^3$-like bonding [37,38], so silicene cannot have a complete planar structure as graphene, even with large strain. We also perceive that the ratio of buckling distance to bond length (nearest-neighbor distance) keeps decreasing with larger strain, which means that the structure becomes more planar under larger strain. The structures of unstrained silicene and silicene under 10% strain are shown in the inset of Fig. 1. It can be clearly seen that strain will reduce the buckling distance and result in longer atomic bond length.

### B. Dispersion

Figure 2 shows the phonon dispersion curve in high-symmetry directions. The phonon dispersion curve plays a crucial role in computing the correct thermal conductivity [39]. Our result for the phonon dispersion curve for unstrained silicene is similar to other first-principles calculations [7,38,40]. Since silicene has a small buckling, its structure does not have reflectional symmetry [41] across the $xy$ plane. As a result, the vibrational pattern of flexural acoustic mode is not purely out-of-plane, as demonstrated in our previous work [42]. Hereafter we denote this flexural acoustic phonon branch as the FA branch to avoid confusion with the purely out-of-plane acoustic (ZA) branch in graphene. Gu and Yang suggested that due to the buckling, the FA branch is not quadratic near the zone center ($q \to 0$). Instead, it has a linear component and therefore a well-defined group velocity [21]. In this work we do see a nonzero group velocity (Fig. 2) for the flexural mode of unstrained silicene near zone center. Considering the limitation on accuracy of first-principles calculation, it is also possible that such a linear behavior is due to the small residue strain in our system [43]. Some argue that the linear or quadratic nature of the flexural mode could qualitatively change the thermal conductivity of 2D materials [43]. Since this is not a major purpose of this work, we later report the result for finite size or finite $q$ mesh, to avoid the argument on this issue. In addition, in the range of 3–6 THz, the longitudinal acoustic (LA) branch and flexural optical (FO) branch have an avoided crossing [44]. This is because the LA and FO modes have the same symmetry, which is again originated from the buckling [45]. This is different from graphene where the out-of-plane optical (ZO) and LA branch cross at about 25 THz (~834 $\text{cm}^{-1}$) [46].

Comparing with the dispersion of unstrained silicene, the dispersion curves of optical phonon modes overall shift downward when the applied tensile strain increases. This shift is mainly due to the reduction of the material stiffness under tensile strain, which is similar to other bulk and low-dimensional materials [47,48]. It is interesting to note that the frequency gap at the avoided crossing is reduced when the tensile strain increases. We believe this can be attributed to the fact that the structure of strained silicene is becoming more planar when a larger strain is applied, as we discussed earlier.

In order to quantify the acoustic phonon group velocity near the zone center, we calculated the group velocities at the Γ point for three acoustic modes. The group velocity of the FA branch increases monotonically from 1075.7 m/s for the unstrained case to 3287.0 m/s for 10% strain. This is related to the increased stiffness in the out-of-plane direction when we apply tensile strain in the in-plane directions. The group velocity of the LA branch decreases monotonically from 9548.3 m/s for the unstrained case to 7184.6 m/s for 10% strain, which is due to the increase in the Si-Si bond length and the weakened Si-Si interatomic interaction in the in-plane directions. For the transverse acoustic (TA) branch, the group velocity first increases from 5629.7 m/s for the unstrained case to 5804.4 m/s for 4% strain, and then slightly decreases to 5235.7 m/s for 10% strain. It should be noted that the strain dependence of the zone center phonon group velocity of silicene is quite different from that of bulk silicon, in which the group velocity only changes slightly under ±3% strain [49]. The strain dependence is quite similar to graphene, where the slope of the ZA branch increases with strain and the LA branch decreases with strain [50].

### C. Thermal conductivity

To ensure the accuracy of our thermal conductivity calculation, convergence tests were first performed with respect to the nearest-neighbor cutoff and then the density of the $q$ mesh. The details and results are presented in the Appendix. We show that for the calculation of anharmonic IFCs, cutoff at fourth-nearest neighbor is enough to achieve converged thermal conductivity values. Regarding the convergence with respect to the $q$ mesh, from our simulation it seems that for infinite size (without boundary scattering), the thermal conductivity tends to diverge with denser $q$ mesh, while for finite size the thermal conductivity will converge. The possible divergence of thermal conductivity for 2D materials has raised a lot of debate recently. For example, in Ref. [21] it was claimed that the thermal conductivity of silicene would diverge with the sample size. Similar conclusions have been drawn in some other literature for graphene [43]. On the other hand, Fugallo *et al.* [50] argue that the thermal conductivity of graphene will converge when the simulated sampling size goes up to 1 mm. In their work, exact phonon BTE is solved and first-principles calculations are employed to extract harmonic and anharmonic IFCs. Barbarino *et al.* [51] also reach the same conclusion with approach-to-equilibrium molecular dynamics simulations for a graphene sample of 0.1 mm in size. Since the major purpose of our work is to discuss the strain effect, we do not intend to argue about this issue. We therefore report the results for a finite $q$ mesh ($101 \times 101 \times 1$ and $201 \times 201 \times 1$) and/or finite sample size (0.3, 3, and 30 $\mu$m). By using a finite $q$ mesh, we actually exclude those extremely long wavelength acoustic phonon modes, which are believed to be responsible for the possible divergence of the thermal conductivity [43]. For finite sample size, the boundary scattering imposes a limit on the phonon mean free path (MFP) to avoid divergence. The results reported below for finite sample sizes are the thermal conductivity values obtained by linearly extrapolating the $q$ mesh to infinity (see the Appendix for more details).

The thermal conductivity values of silicene at 300 K under different tensile strains are computed with both RTA and the iterative method, as shown in Fig. 3. The results of infinite (here "infinite" refers to the case without boundary scattering but has a finite $q$ mesh, similarly for the subsequent discussions) unstrained silicene for the $201 \times 201 \times 1$ $q$ mesh are 33.8 and 36.2 W/mK for RTA and the iterative method, respectively. We note that RTA and the iterative method give similar values of thermal conductivity and similar trends in the strain dependence. For infinite size, both methods predict that thermal conductivity first increases significantly and then decreases slightly. For different $q$ mesh the strain dependence is also similar. The highest thermal conductivity value (for $201 \times 201 \times 1$, RTA, 242.5 W/mK) appears at 4% strain and is about 7 times that of the unstrained case. Such a significant increase is quite anomalous. Usually the thermal conductivity of bulk materials, such as silicon [49], diamond [52], and argon [53] would only slightly decrease under tensile strain. For graphene, a similar method predicted that the thermal conductivity only slightly increases with 4% strain [50,54]. In some other empirical molecular dynamics based calculations, it was even found that the thermal conductivity of graphene decreases with tensile strain [47]. With all the strains we considered, the maximum thermal conductivity occurs at 4% strain, which is the turning point where buckling distance of silicene does not decrease significantly with strain any more. This implies that the thermal conductivity of silicene has a strong correlation with the buckling distance. In the literature it is also suggested that at 7.5% strain silicene becomes metallic [25], where electrons may also contribute to the total thermal conductivity. In our calculation, we considered the contribution of phonons to the thermal conductivity only.

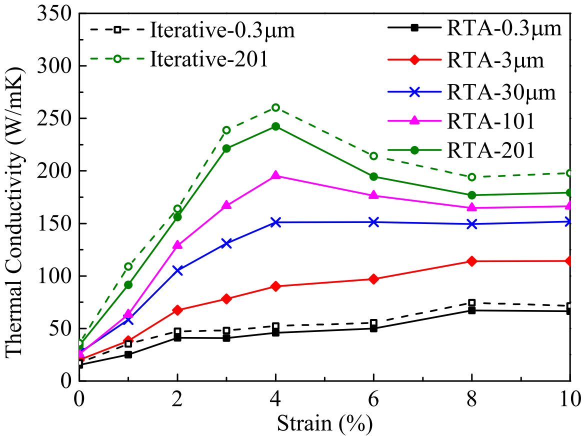

FIG. 3. Thermal conductivity of infinite ($101 \times 101 \times 1$ and $201 \times 201 \times 1$ $q$ mesh) and finite-size (0.3, 3, and 30 $\mu$m) silicene as a function of strain computed with RTA and iterative method. Note that since RTA and iterative method give similar thermal conductivity values for different cases, we only show the iterative results for the $201 \times 201 \times 1$ infinite and the 0.3 $\mu$m size cases.

For the three finite-size cases the thermal conductivity of unstrained silicene is in the range of 15 to 30 W/mK, as listed in Table I. These results agree well with the prediction by Gu *et al.* [21] in which the thermal conductivity of unstrained silicene is predicted to be around 23 W/mK for

TABLE I. Thermal conductivity of unstrained silicene and the tunability.

| | RTA | | Iterative method | |
|---|---|---|---|---|
| Size | $k_l^0$ (W/mK) | Tunability | $k_l^0$ (W/mK) | Tunability |
| 0.3 $\mu$m | 15.2 | 4.4 | 17.3 | 4.3 |
| 3 $\mu$m | 20.1 | 5.7 | 22.4 | 5.8 |
| 30 $\mu$m | 26.9 | 5.6 | 29.3 | 5.8 |

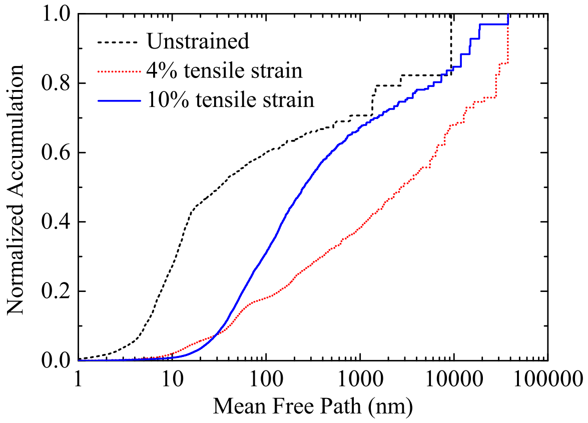

FIG. 4. Normalized thermal conductivity accumulation function with respect to phonon mean free path for 0%, 4%, and 10% strain.

3 $\mu$m size. For all the sample sizes we considered, the thermal conductivity increases dramatically with strain, although the highest thermal conductivity appears at different strain values. The tunability within 10% strain (defined as the ratio of the largest thermal conductivity of strained silicene and the unstrained one) is smaller than the infinite case, but is still quite large. For the 0.3 $\mu$m case, the tunability is about 4.3 and is the smallest, as shown in Table I.

To understand the size dependence on the tunability, we further plot the normalized thermal conductivity accumulation function $k_{acc}(\Lambda_0)/k_l^{xx}$ for the 0%, 4%, and 10% strained silicene (using $101 \times 101 \times 1$ $q$ mesh), as shown in Fig. 4. It can be seen that although for the infinite case 4% strain gives the largest thermal conductivity, a significant amount is contributed by phonons with relatively long MFP. In contrast, for the 10% strained case, the thermal conductivity is contributed by relatively shorter MFP phonons. Since the sample size limits the maximum MFP, finite size actually has a more significant effect on the thermal conductivity of 4% strain than 10% strain. This explains why the strain dependence is different for different sample sizes.

As can be seen from the discussions above, the major anomalous behavior is the significant increase of thermal conductivity with tensile strain, which is seen in both finite-size and infinite cases. The strain dependence of the finite samples arises from the combination of the unusual strain dependence of infinite samples (with finite $q$ mesh) and the effect of boundary scattering. Actually the most important issue is to understand the strain dependence of infinite samples. As such, we choose the RTA result with infinite size in the subsequent discussions to explore the mechanism for this anomalous behavior of silicene. Also, we consider the $101 \times 101 \times 1$ $q$ mesh, to preserve the essential physics but also reduce the number of data points in the subsequent figures.

### D. Contribution from different branches

To understand the anomalous strain dependence of thermal conductivity, we first decompose the thermal conductivity contributions into different phonon modes, and the results are also plotted in Fig. 5. Different phonon modes are sorted by their frequencies. The lowest branch is taken as the FA branch while the highest three branches are taken as optical branches. The other two branches are then TA or LA branch. This is a simple and commonly used method to sort different phonon modes in the entire Brillouin zone. We have carefully checked the symmetry of eigenvectors and find this algorithm is reliable for almost all the phonons except at a few high-symmetry points. It is evident that the acoustic branches give the dominant contribution over the full strain range, while contribution from optical phonons is in the range of 4%–22%. The percentage of optical phonon contribution is similar to silicon nanowires [55]. Figure 5 also shows that LA and TA modes contribute more than half of the total thermal conductivity and govern the trend of strain dependence of thermal conductivity. Especially when the strain is smaller than 4%, TA and LA modes contribute more than 65% of the total thermal conductivity. This is quite different from graphene, for which it is believed that the pure out-of-plane ZA mode has a major contribution to the total thermal conductivity [2,41,56]. The thermal conductivity contributed by the FA mode first increases with strain up to 6% and then slightly decreases. At zero strain, the contribution from the FA mode is only about 5% while at 6% strain the contribution from the FA mode increases up to around 45%.

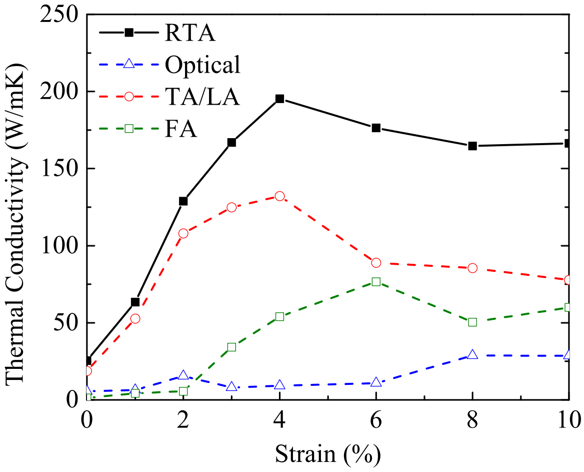

FIG. 5. The branch contribution of optical phonons, TA/LA phonons, and FA phonons to the total thermal conductivity computed with RTA.

### E. Heat capacity, group velocity, and lifetime

From Eq. (3) we know that thermal conductivity is related to volumetric phonon specific heat (heat capacity) $c_{ph}$, group velocity $v_x$, and phonon lifetime $\tau$. In order to find out the dominant factor for the anomalous strain dependence of thermal conductivity, we substitute each of the three terms for unstrained silicene with the value of strained silicene. For example, when heat capacity is replaced, the thermal conductivity is calculated as

$$k_l^{xx,\epsilon} = \frac{1}{N}\sum_{\lambda} c_{ph,\lambda}^{\epsilon}\left(v_{x,\lambda}^{0}\right)^2 \tau_{\lambda}^{0}. \tag{8}$$

The results for three cases are plotted in Fig. 6. We see that the calculated thermal conductivity changes significantly

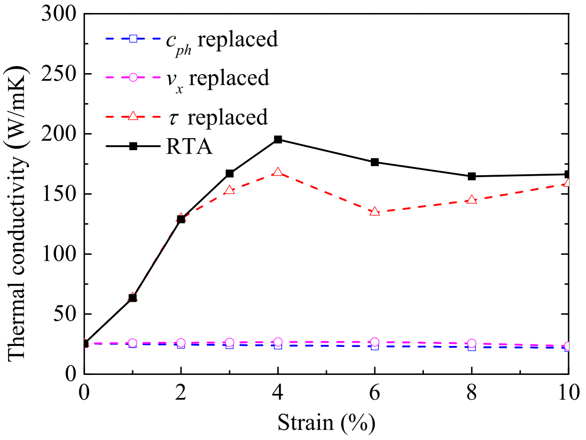

FIG. 6. Thermal conductivity as a function of strain computed with RTA and cross-calculated thermal conductivity with $c_{ph}$, $v_x$, or $\tau$ replaced with strained values.

when lifetime is replaced with the value of strained silicene. At 4% strain, the highest value is about 7 times that of unstained case. This shows that the unusual strain dependence of thermal conductivity is mainly due to the change in phonon lifetime. From 0% to 6% strain the thermal conductivity with lifetime replaced changes dramatically, indicating that lifetime is the dominant factor in this range of strain. From 6% to 10% strain the thermal conductivity with lifetime replaced changes about 17.8%, while the thermal conductivity with group velocity or heat capacity replaced changes $-12.7\%$ and $-5.7\%$ respectively. In this range of strain, these changes are on the same order of magnitude. The three competing factors balance in this range, so the change in the thermal conductivity is small.

### F. Lifetime

To further quantify the lifetime variation under different strains, we plotted the frequency-dependent phonon lifetime in Fig. 7. Since acoustic phonons are the dominant heat carriers in the thermal transport in silicene, we only show the lifetimes for acoustic phonons. In addition, those negligible phonon modes whose aggregate contribution to thermal conductivity is less than 0.1% are excluded to reduce the number of data points. From Fig. 7 it can be seen that, except for a few phonon modes, the acoustic phonon lifetimes of strained silicene are consistently significantly larger than that of unstrained case. The top panel in Fig. 7 indicates that the overall FA phonon lifetimes keep increasing for strain from 0% to 6% but decrease a little for strain from 6% to 10%. The major heat carriers whose aggregate contribution to overall thermal conductivity is more than 50% are those low-frequency acoustic phonons with frequencies under 2.8 THz. The bottom panel shows that the lifetime of TA/LA phonons with frequencies lower than 2.8 THz would overall increase when silicene is strained from 0% to 4%, and then decrease afterwards. The transition from increased to slightly decreased lifetime occurs in the range of 4%–6% strain for all the important acoustic phonon modes, which is consistent with the strain-dependent thermal conductivity. It should be noted that such a significant change in phonon lifetime with tensile strain is quite unusual. In Ref. [49], the strain-dependent phonon lifetime for solid argon and silicon was calculated using a similar approach. The phonon lifetimes of both materials show quite small strain dependence (changes are within 300%). Here for silicene, the phonon lifetime of the majority of low-frequency FA phonons increases by two to three orders of magnitude with strain and the variation of TA/LA lifetime is also one to two orders of magnitude.

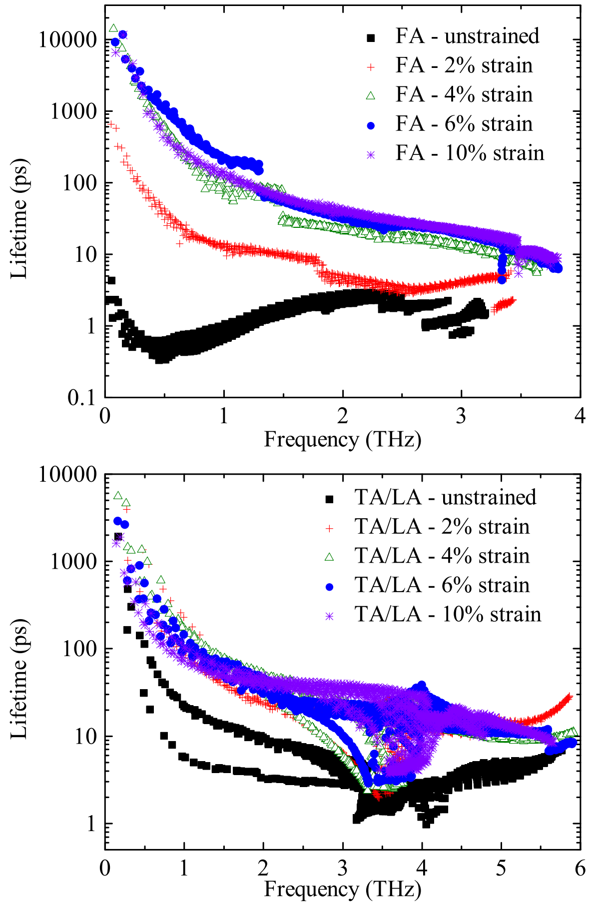

FIG. 7. Top panel: Lifetime of FA phonons as a function of frequency for 0%, 2%, 4%, 6%, and 10% strain. Bottom panel: Lifetime of LA/TA phonons as a function of frequency for 0%, 2%, 4%, 6%, and 10% strain.

### G. Weighted phase space and scattering channel

To understand such a dramatic change of acoustic phonon lifetime, we also calculated the phase space defined in Ref. [57] and the "weighted phase space" defined in Ref. [58] (results not shown). The weighted phase space is an expression of frequency-containing factors that quantifies the phonon scattering probability for a particular dispersion curve. The weighted phase space was used to successfully explain the ultralow thermal conductivity of filled skutterudite $\mathrm{YbFe_4Sb_{12}}$ [58]. However, unlike $\mathrm{YbFe_4Sb_{12}}$ whose low thermal conductivity is mainly attributed to the allowed phase space for scattering, the variation of weighted phase space of silicene under different strains cannot fully explain the large variation of phonon lifetime. We also calculated

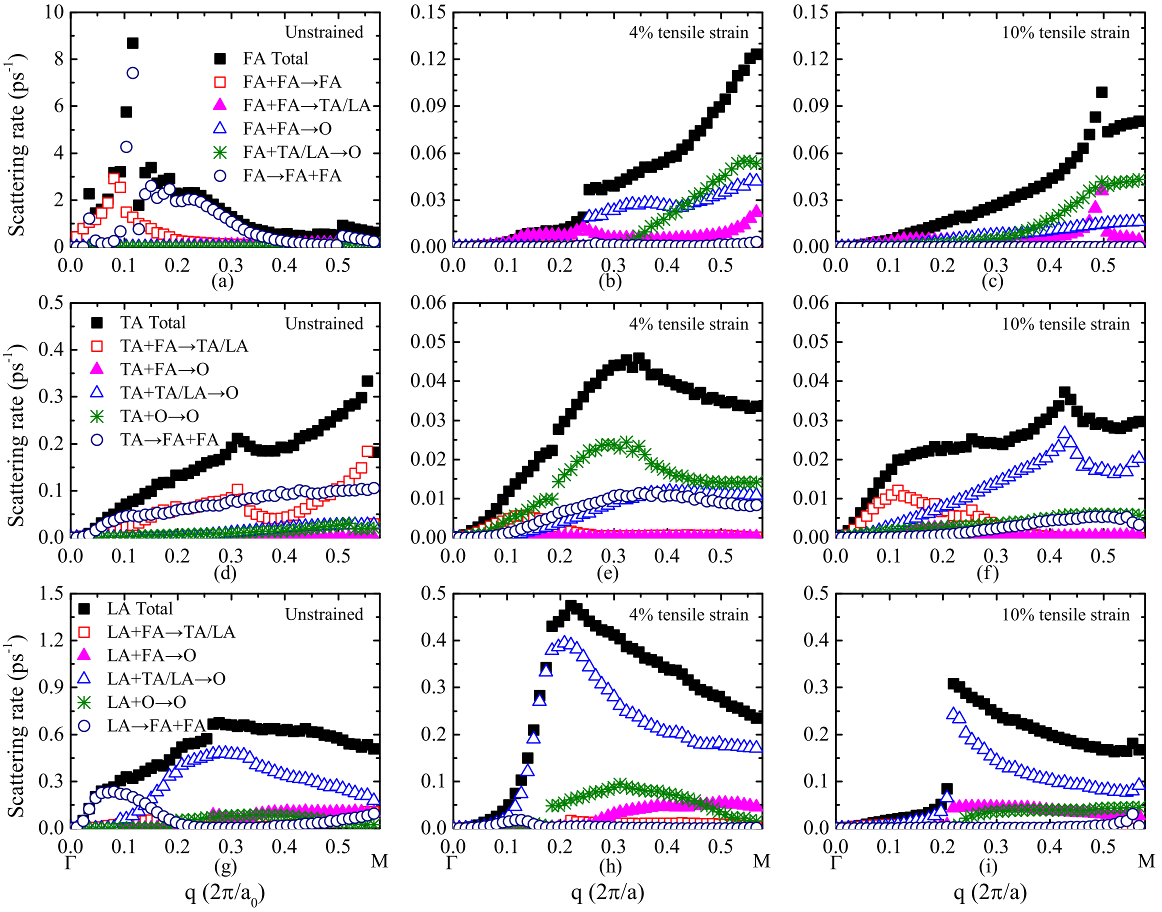

FIG. 8. Scattering rates of acoustic phonons from Γ to M: FA phonons for (a) unstrained silicene, (b) 4% strained silicene, (c) 10% strained silicene. TA phonons for (d) unstrained silicene, (e) 4% strained silicene, (f) 10% strained silicene. LA phonons for (g) unstrained silicene, (h) 4% strained silicene, (i) 10% strained silicene. (Please note the difference in the scales for scattering rates in the panels.)

thermal conductivity using the harmonic IFCs of 4% strain and anharmonic IFCs with 0% strain; the result is only about twice the unstrained thermal conductivity. Together with the calculation result of weighted phase space, we find that the variation of neither harmonic nor anharmonic IFCs alone can fully account for the variation of phonon lifetime.

We further investigate the different scattering channels to quantify the importance of different phonon modes in the scattering processes. Figure 8 shows the scattering rates of acoustic phonons along the Γ to M direction, and only major scattering channels that have a large contribution to overall scattering rate are included. Scattering rates for emission processes are multiplied by $1/2$ to avoid counting the same process twice. Note that along the Γ to M direction the FA, TA, and LA branches can be easily separated, so the scattering channels for the three branches are plotted separately in Fig. 8.

Figures 8(a)–8(c) show the scattering rates of different scattering channels of FA phonons for unstrained (0%), 4%, and 10% strained silicene, respectively. Note that the legends are the same for these three panels while the scales for the $y$ axis are not the same. It can be seen that the total scattering rates of FA phonons decrease orders of magnitude from 0% to 4% but decrease only a little from 4% to 10%. In unstrained silicene, dominant scattering channels are those among FA modes (i.e., FA+FA → FA and FA → FA+FA processes). However for strained silicene, either 4% or 10%, the dominant scattering channels become FA+FA → TA/LA, FA+FA → O, and FA+TA/LA → O, where O indicates optical phonons. The scattering among FA phonons is significantly reduced. Our data also show that the scattering rates of FA+TA/LA → O processes decrease from 0% to 4% strain. We attribute the decrease of scattering rates for processes involving odd number of FA phonons to the change of buckling distance. For graphene, because of the reflectional symmetry of the structure, the phonon scattering process involving an odd number of ZA phonons is not allowed, leading to a very small scattering rate of the ZA mode [41]. Our observation of the FA mode is in line with the discussion on graphene: when strain is larger, the silicene structure becomes more planar, so the scattering rates of processes involving an odd number of FA modes (especially the scattering process involving 3 FA modes) decrease.

As we noted before, the dramatic change of thermal conductivity from 0% to 4% is mainly due to the in-plane modes (TA and LA). Therefore, we need to further check the scattering channel of TA and LA modes. Figures 8(d)–8(f) plot the scattering rates of TA phonons for 0%, 4%, and 10% strained silicene, respectively. Similarly to the trend of FA phonons, the total scattering rates reduce significantly from 0% to 4% strain. From 4% to 10% strain, scattering rates still decrease slightly in the high-frequency region but increase in the low-frequency region. For unstrained silicene, dominant scattering channels are TA+FA → TA/LA and TA → FA+FA. For silicene under 4% tensile strain, dominant scattering channels are TA+O → O, TA+TA/LA → O, and TA → FA+FA. For silicene under 10% strain, dominant scattering channels become TA+TA/LA → O and TA+FA → TA/LA. The variation of scattering rates for different scattering channels for TA phonon modes are the most complicated. The scattering rates of the common dominant process TA → FA+FA become smaller with larger strain. For the TA+TA/LA → O process, the scattering rates increase. For TA+O → O, the scattering rates first become larger from 0% to 4%, and then become smaller from 4% to 10%. For TA+FA → TA/LA, the trend is opposite to the previous one: scattering rates first become smaller then become larger. Overall, we find that with larger strain the scattering with the FA phonon becomes weaker while the scattering with the optical phonon becomes stronger. These competing mechanisms result in the change of the total scattering rates.

Figures 8(g)–8(i) at the bottom are the scattering rates of LA phonons for 0%, 4%, and 10% strained silicene, respectively. The total scattering rates of LA phonons decrease monotonically from 0% to 4% and then to 10% strain, but we also note that the total scattering rates of LA phonons do not change as much as FA and TA modes. For different strains LA+TA/LA → O is the dominant scattering channel for all the three cases, presumably due to the relatively higher frequency of LA modes. At the low-frequency region of the unstrained case, LA → FA+FA is dominant, but at larger strain this channel is becoming less important.

From the analysis of the scattering channel, we have a few observations. First, the scattering among FA modes is significantly reduced with larger tensile strain, which is due to the reduced buckling distance and more planar structure. This could explain the significant enhancement of phonon lifetime for FA modes as seen in Fig. 7. We should note that this is not the major reason for the enhanced thermal conductivity from 0% to 4% strain, because FA modes have relatively small contributions to thermal conductivity in this range. Second, the scattering rates of TA modes decrease significantly from 0% to 4% strain, mainly due to the reduced scattering with FA modes. This is the major factor why the thermal conductivity of silicene increases in this range. Third, the LA phonon scattering rates do not change significantly under different strains and thus are not responsible much to the large tunability of thermal conductivity. Lastly, we should note that the above analysis is based on the Γ to M region of the Brillouin zone. To distinguish TA and LA phonons is not always possible for any $q$ point, so it is not safe to conclude that the enhanced thermal conductivity is mainly due to TA modes. We rather believe that the enhanced thermal conductivity is mainly due to the enhanced lifetime of both LA and TA modes because they scatter less with FA modes when strain is applied.

## IV. SUMMARY

In conclusion, we performed first-principles calculations to predict the lattice thermal conductivity of silicene under strain. Phonon BTE is solved both in the RTA scheme and iteratively in our prediction. Both methods yield similar trends in the change of thermal conductivity with respect to tensile strain. It is shown that within 10% tensile strain the thermal conductivity of silicene can increase dramatically. Such a dramatic change is quite unusual for solid materials, and could be used as a thermal switch together with thermal diodes to build thermal circuits. This trend is mainly due to the strain-dependent phonon lifetime, which is related to the variations of both harmonic and anharmonic IFCs under strain. FA phonon lifetimes increase significantly under tensile strain because the structure becomes more planar. This leads to a large increase of their contribution to overall thermal conductivity, but is not the major reason for the significant change of overall thermal conductivity within 4% strain. The significant enhancement of thermal conductivity from 0% to 4% strain is mainly due to the reduced scattering of TA and LA phonons with FA phonons. Our result suggests that other 2D materials with intrinsic buckling may have similar strain dependence of thermal conductivity, which is left for further investigation.

## ACKNOWLEDGMENTS

This work was supported by the National Natural Science Foundation of China (Grant No. 51306111) and Shanghai Municipal Natural Science Foundation (Grant No. 13ZR1456000). M.H. acknowledges support by the Deutsche Forschungsgemeinschaft (DFG) (Project No. HU 2269/2-1). Simulations were performed with computing resources granted by HPC ($\pi$) from Shanghai Jiao Tong University. The authors thank Dr. Wu Li for answering questions regarding ShengBTE.

## APPENDIX: CONVERGENCE TESTS

In order to ensure that the thermal conductivity is well converged, we first justify our results with respect to the number of nearest neighbors included in computing anharmonic IFCs. Figure 9 shows the thermal conductivity of infinite (without boundary scattering) unstrained silicene calculated

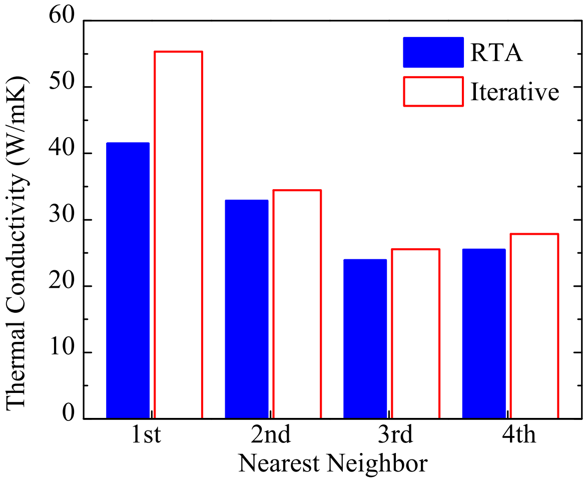

FIG. 9. Thermal conductivity of unstrained silicene vs nearest neighbors computed with RTA and iterative method.

with a $101\times101\times1$ $q$ mesh. It can be seen that when more neighboring atoms are included, the thermal conductivity first decreases and then converges. With the fourth-nearest neighbors included, the results are 25.5 and 27.9 W/mK for RTA and the iterative method respectively. Including up to the third-nearest neighbors only slightly changes the results (less than 10%) for both RTA and the iterative method. We notice that in our previous first-principles calculation [20], the thermal conductivity of 9.4 W/mK is much smaller. This is attributed to two reasons: (i) We only included the first-nearest neighbors to compute the anharmonic IFCs. (ii) We did not impose the sum rule [22,29] to anharmonic IFCs. As we have mentioned, up to fourth-nearest neighbors are included with a $5\times5\times1$ supercell in this work and converged results are achieved. When computing anharmonic IFCs, the following sum rule is enforced in the THIRDORDER.PY package by adding a small compensation to independent nonzero terms [29]:

$$\sum_k \Phi_{ijk}^{\alpha\beta\gamma} = 0, \tag{A1}$$

where $\Phi$ is the anharmonic IFC, and $i, j$, and $k$ are the atom indices. $\alpha$, $\beta$, and $\gamma$ denote the $x$, $y$, or $z$ direction. The sum of the square of the compensation terms is minimized to ensure that the other symmetries are still satisfied [29].

In addition, a convergence test was performed with respect to $q$-mesh density. Figure 10(a) shows the thermal conductivity of infinite unstrained silicene and finite-size (3 $\mu$m and 30 $\mu$m) unstrained silicene with different $q$-mesh density. Figure 10(b) shows the thermal conductivity of infinite 4% strained silicene and finite-size (3 $\mu$m and 30 $\mu$m) 4% strained silicene with different $q$-mesh density. The solid lines are the results of RTA and the dashed lines are those of the iterative method. All the results are obtained with an $N_1\times N_1\times1$ $q$ mesh ($N_1 = 51$, 101, 151, and 201). Both RTA and the iterative method show possibly diverged thermal conductivity for infinite size. For finite-size unstrained and 4% strained silicene, the results with $L_x = 3$ $\mu$m and 30 $\mu$m are shown. Both methods show converged results and we extrapolate them to infinite $q$-mesh density with a linear relationship fitted between $k$ and $1/N_1$. The convergence study for unstrained silicene reaches essentially the same conclusion as the work by Gu and Yang [21]. Similar convergence tests were performed for all the strained cases and we consistently found a possibly diverged thermal conductivity for the infinite case and converged results for finite sizes. Due to the limited space we did not shown all the results here.

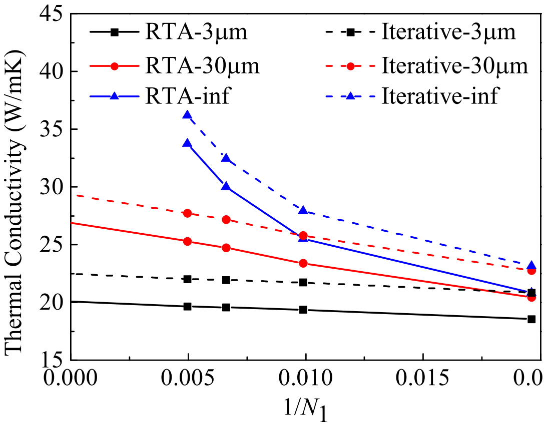

(a) Unstrained silicene

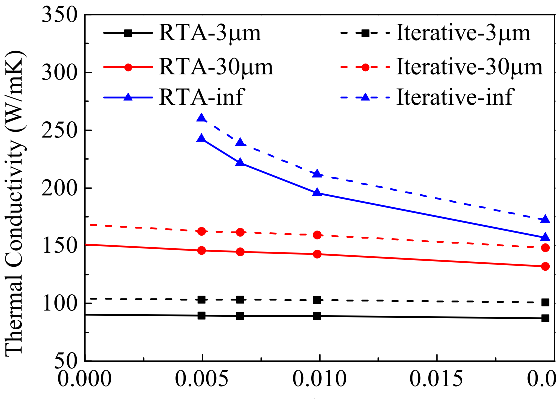

(b) 4% strained silicene

FIG. 10. Thermal conductivity of unstrained silicene for different $q$ mesh and different sizes computed with RTA and iterative method.

---

[1] K. S. Novoselov, A. K. Geim, S. V. Morozov, D. Jiang, Y. Zhang, S. V. Dubonos, I. V. Grigorieva, and A. A. Firsov, Science **306**, 666 (2004).

[2] J. H. Seol, I. Jo, A. L. Moore, L. Lindsay, Z. H. Aitken, M. T. Pettes, X. Li, Z. Yao, R. Huang, D. Broido, N. Mingo, R. S. Ruoff, and L. Shi, Science **328**, 213 (2010).

[3] R. Yan, J. R. Simpson, S. Bertolazzi, J. Brivio, M. Watson, X. Wu, A. Kis, T. Luo, A. R. Hight Walker, and H. G. Xing, ACS Nano **8**, 986 (2014).

[4] J. D. Renteria, D. L. Nika, and A. A. Balandin, Appl. Sci. **4**, 525 (2014).

[5] L. Tao, E. Cinquanta, D. Chiappe, C. Grazianetti, M. Fanciulli, M. Dubey, A. Molle, and D. Akinwande, Nat. Nanotechnol. **10**, 227 (2015).

[6] A. A. Balandin, S. Ghosh, W. Bao, I. Calizo, D. Teweldebrhan, F. Miao, and C. N. Lau, Nano Lett. **8**, 902 (2008).

[7] N. D. Drummond, V. Zólyomi, and V. I. Fal'ko, Phys. Rev. B **85**, 075423 (2012).

[8] Z. Ni, Q. Liu, K. Tang, J. Zheng, J. Zhou, R. Qin, Z. Gao, D. Yu, and J. Lu, Nano Lett. **12**, 113 (2012).

[9] T. P. Kaloni, Y. C. Cheng, and U. Schwingenschlögl, J. Appl. Phys. **113**, 104305 (2013).

[10] B. Aufray, A. Kara, S. Vizzini, H. Oughaddou, C. Léandri, B. Ealet, and G. L. Lay, Appl. Phys. Lett. **96**, 183102 (2010).

[11] L. Meng, Y. Wang, L. Zhang, S. Du, R. Wu, L. Li, Y. Zhang, G. Li, H. Zhou, W. A. Hofer, and H.-J. Gao, Nano Lett. **13**, 685 (2013).

[12] B. Lalmi, H. Oughaddou, H. Enriquez, A. Kara, S. Vizzini, B. Ealet, and B. Aufray, Appl. Phys. Lett. **97**, 223109 (2010).

[13] N.-T. Nguyen, Micro Nanosyst. **6**, 205 (2014).

[14] C. Lian and J. Ni, Phys. Chem. Chem. Phys. **17**, 13366 (2015).

[15] F. Schwierz, J. Pezoldt, and R. Granzner, Nanoscale **7**, 8261 (2015).
[16] H.-p. Li and R.-q. Zhang, Europhys. Lett. **99**, 36001 (2012).
[17] T. Y. Ng, J. Yeo, and Z. Liu, Int. J. Mech. Mater. Des. **9**, 105 (2013).
[18] Q.-X. Pei, Y.-W. Zhang, Z.-D. Sha, and V. B. Shenoy, J. Appl. Phys. **114**, 033526 (2013).
[19] M. Hu, X. Zhang, and D. Poulikakos, Phys. Rev. B **87**, 195417 (2013).
[20] H. Xie, M. Hu, and H. Bao, Appl. Phys. Lett. **104**, 131906 (2014).
[21] X. Gu and R. Yang, J. Appl. Phys. **117**, 025102 (2015).
[22] L. Lindsay, D. A. Broido, and T. L. Reinecke, Phys. Rev. B **87**, 165201 (2013).
[23] S. Bhowmick and V. B. Shenoy, J. Chem. Phys. **125**, 164513 (2006).
[24] J.-A. Yan, S.-P. Gao, R. Stein, and G. Coard, Phys. Rev. B **91**, 245403 (2015).
[25] G. Liu, M. S. Wu, C. Y. Ouyang, and B. Xu, Europhys. Lett. **99**, 17010 (2012).
[26] C. Lian and J. Ni, AIP Adv. **3**, 052102 (2013).
[27] M. I. Baskes, Phys. Rev. B **46**, 2727 (1992).
[28] J. Tersoff, Phys. Rev. B **39**, 5566 (1989).
[29] W. Li, J. Carrete, N. A. Katcho, and N. Mingo, Comput. Phys. Commun. **185**, 1747 (2014).
[30] J. E. Turney, E. S. Landry, A. J. H. McGaughey, and C. H. Amon, Phys. Rev. B **79**, 064301 (2009).
[31] G. P. Srivastava, *The Physics of Phonons* (Adam Hilger, Bristol, 1990).
[32] A. J. McGaughey, E. S. Landry, D. P. Sellan, and C. H. Amon, Appl. Phys. Lett. **99**, 131904 (2011).
[33] G. Kresse and J. Furthmüller, Comput. Mater. Sci. **6**, 15 (1996).
[34] P. E. Blöchl, Phys. Rev. B **50**, 17953 (1994).
[35] J. P. Perdew, K. Burke, and M. Ernzerhof, Phys. Rev. Lett. **77**, 3865 (1996).
[36] A. Togo, F. Oba, and I. Tanaka, Phys. Rev. B **78**, 134106 (2008).
[37] S. Cahangirov, M. Topsakal, E. Aktürk, H. Sahin, and S. Ciraci, Phys. Rev. Lett. **102**, 236804 (2009).
[38] H. Şahin, S. Cahangirov, M. Topsakal, E. Bekaroglu, E. Akturk, R. T. Senger, and S. Ciraci, Phys. Rev. B **80**, 155453 (2009).
[39] L. Paulatto, F. Mauri, and M. Lazzeri, Phys. Rev. B **87**, 214303 (2013).
[40] E. Scalise, M. Houssa, G. Pourtois, B. v. d. Broek, V. Afanasév, and A. Stesmans, Nano Res. **6**, 19 (2012).
[41] L. Lindsay, D. A. Broido, and N. Mingo, Phys. Rev. B **82**, 115427 (2010).
[42] X. Zhang, H. Xie, M. Hu, H. Bao, S. Yue, G. Qin, and G. Su, Phys. Rev. B **89**, 054310 (2014).
[43] N. Bonini, J. Garg, and N. Marzari, Nano Lett. **12**, 2673 (2012).
[44] O. Delaire, J. Ma, K. Marty, A. F. May, M. A. McGuire, M.-H. Du, D. J. Singh, A. Podlesnyak, G. Ehlers, M. D. Lumsden, and B. C. Sales, Nat. Mater. **10**, 614 (2011).
[45] M. T. Dove, *Introduction to Lattice Dynamics* (Cambridge University Press, Cambridge, 1993).
[46] J.-A. Yan, W. Y. Ruan, and M. Y. Chou, Phys. Rev. B **77**, 125401 (2008).
[47] X. Li, K. Maute, M. L. Dunn, and R. Yang, Phys. Rev. B **81**, 245318 (2010).
[48] R. C. Picu, T. Borca-Tasciuc, and M. C. Pavel, J. Appl. Phys. **93**, 3535 (2003).
[49] K. D. Parrish, A. Jain, J. M. Larkin, W. A. Saidi, and A. J. H. McGaughey, Phys. Rev. B **90**, 235201 (2014).
[50] G. Fugallo, A. Cepellotti, L. Paulatto, M. Lazzeri, N. Marzari, and F. Mauri, Nano Lett. **14**, 6109 (2014).
[51] G. Barbarino, C. Melis, and L. Colombo, Phys. Rev. B **91**, 035416 (2015).
[52] D. A. Broido, L. Lindsay, and A. Ward, Phys. Rev. B **86**, 115203 (2012).
[53] A. Chernatynskiy and S. R. Phillpot, J. Appl. Phys. **114**, 064902 (2013).
[54] Y. Kuang, L. Lindsay, and B. Huang, Nano Lett. **15**, 6121 (2015).
[55] Z. Tian, K. Esfarjani, J. Shiomi, A. S. Henry, and G. Chen, Appl. Phys. Lett. **99**, 053122 (2011).
[56] L. Lindsay, D. A. Broido, and N. Mingo, Phys. Rev. B **83**, 235428 (2011).
[57] L. Lindsay and D. A. Broido, J. Phys.: Condens. Matter **20**, 165209 (2008).
[58] W. Li and N. Mingo, Phys. Rev. B **91**, 144304 (2015).